Glass formation in binary alloys with different atomic symmetries

Yuan-Chao Hu ◉,[1] Kai Zhang ◉,[2] Sebastian A. Kube ◉,[1] Jan Schroers,[1] Mark D. Shattuck,[3] and Corey S. O'Hern[1,4,5,*]

[1]*Department of Mechanical Engineering & Materials Science, Yale University, New Haven, Connecticut 06520, USA*
[2]*Division of Natural and Applied Sciences, Duke Kunshan University, Kunshan, Jiangsu, 215300, China*
[3]*Benjamin Levich Institute and Physics Department, The City College of New York, New York, New York 10031, USA*
[4]*Department of Physics, Yale University, New Haven, Connecticut 06520, USA*
[5]*Department of Applied Physics, Yale University, New Haven, Connecticut 06520, USA*

Prediction of the glass-forming ability (GFA) of alloys remains a major challenge. We are not yet able to predict the composition dependence of the GFA of even binary alloys. To investigate the effect of each element's propensity to form particular crystal structures on glass formation, we focus on binary alloys composed of elements with the same size but different atomic symmetries using the patchy-particle model. For mixtures with atomic symmetries that promote different crystal structures, the minimum critical cooling rate R_c is only a factor of 5 lower than that for the pure substances. For mixtures with different atomic symmetries that promote local crystalline and icosahedral order, the minimum R_c is more than three orders of magnitude lower than that for pure substances. Results for R_c for the patchy-particle model are consistent with those from embedded atom method simulations and sputtering experiments of NiCu, TiAl, and high entropy alloys.

I. INTRODUCTION

Bulk metallic glasses (BMGs), which are multicomponent alloys with disordered atomic-scale structure, are a promising materials class because they combine metal-like strength with plasticlike processability [1,2]. Despite their tremendous potential, they have not been widely used, most likely because current BMGs do not combine multiple advantageous properties, such as high strength, high fracture toughness, and low material cost [3–6].

A key first step in the BMG design process is the ability to predict the glass-forming ability (GFA) or the critical cooling rate R_c below which crystallization occurs. To date, BMGs with good GFA, e.g., $Pd_{42.5}Cu_{30}Ni_{7.5}P_{20}$ with $R_c \sim 10^{-2}$ K/s, have been identified mainly through time-consuming experiments that are guided by empirical rules [7,8]. The number of multicomponent alloys that can potentially form metallic glasses is enormous, i.e., more than 10^6 if we consider four-component alloys with 32 possible elements and 1% increments in composition of each of the four elements [6]. However, even using the latest high-throughput sputtering techniques, researchers can only characterize a minute fraction of the potential BMG-forming alloys [9–12].

An important goal is to develop a computational platform to predict the GFA of alloys. One approach could involve using *ab initio* molecular dynamics (MD) or embedded atom method (EAM) simulations to directly measure R_c for each alloy [13]. However, such simulations are computationally demanding, e.g., EAM simulations can typically only achieve cooling rates $\geqslant 10^9$ K/s with current computational capa-

bilities. Even more, it is not presently known what level of description is required to achieve a desired accuracy in the prediction of R_c. For example, do we need to track the electronic degrees of freedom of alloys or can we use effective pairwise or three-body interactions to obtain accurate predictions of the GFA? Further, EAM potentials have only been developed for a small fraction of the possible alloys and it is currently not known whether existing EAM potentials can accurately recapitulate the experimentally measured GFA of these alloys.

In this paper, we begin laying the foundation for a theoretical approach to predict the GFA of alloys. We focus on binary systems (with elements A and B) and determine whether the best GFA for the alloy occurs for equal proportions of A and B or whether the best GFA occurs for the A- or B-rich systems via MD simulations. The answer to even this simple question is unknown for most binary alloys. The central hypothesis of this paper is that the GFA of binary alloys can be described by functions of combinations of features of the elements A and B that make up the alloy. Example *elemental* features include the cohesive energies of the elements, ϵ_A and ϵ_B, and the atomic diameters σ_A and σ_B [14–18]. In this paper, we consider an additional feature: the atomic symmetry or the propensity of an element to form a particular crystalline phase or to form icosahedral (ICO) short-range order. For example, Ni and Cu possess face-centered cubic (fcc) atomic symmetry, whereas, Fe and Cr possess body-centered cubic (bcc) atomic symmetry. For these elements, the pure metals will form fcc or bcc crystalline phases even at extremely high cooling rates. However, other pure metals, such as Al, possess much lower critical cooling rates and will only crystallize at low cooling rates [19,20]. Recent numerical studies [21] have shown that interatomic potentials with two competing

———————
[*]corey.ohern@yale.edu

length scales, e.g., one that has a minimum at small atomic separations and a maximum at larger separations, can give rise to quasicrystal formation, especially at elevated cooling rates. In particular, these researchers performed MD simulations using an EAM potential for pure Al that possesses multiple local minima in the effective pair potential. They showed that when pure Al was rapidly cooled from the liquid state to low temperatures, quasicrystals with ICO symmetry form. However, experiments have not confirmed that pure Al can form quasicrystals, and thus additional experiments measuring the structure of rapidly cooled Al, as well as other pure metals, are necessary.

To isolate the effect that atomic symmetry has on glass formation, we developed an effective patchy-particle potential to model the behavior that some pure metals can form fcc, bcc, or hcp (hexagonal closest packed) crystals even at high cooling rates, whereas other pure metals must be cooled extremely slowly to form crystalline phases [22–24]. This feature is implemented in the simulations by choosing the form of the patchy interaction potential for each element. For example, an fcc, hcp, or ICO atom has 12 patches positioned on the atom surface to generate either fcc, hcp, or ICO symmetry, and a bcc atom has eight patches positioned on the atom surface to generate bcc symmetry. This effective patchy potential captures an elemental feature that drives a system to form a particular solid phase with a given local or global symmetry. To simplify the problem, we considered systems with different cohesive energies and atomic symmetries but the same atomic size, $\sigma_A/\sigma_B = 1.0$. We argue below that the patchy-particle model can describe the GFA for binary alloys with similar atomic sizes, phase diagrams that do not possess any eutectic points, and thus a composition-dependent melting temperature that is largely monotonic. In future studies, the patchy-particle model can be used to describe the GFA of a wider range of binary and ternary alloys composed of elements with different atomic sizes, as well as different cohesive energies.

To motivate the use of the patchy-particle model for describing the GFA of binary alloys, we first performed EAM MD simulations to calculate the composition-dependent R_c for two binary alloys, NiCu and TiAl. We find that even though these pairs of elements have approximately the same atomic sizes, they possess very different composition-dependent GFAs. In particular, for NiCu alloys, R_c depends only weakly on composition, whereas the composition-dependent GFA for TiAl varies by more than three orders of magnitude. This behavior is related to the propensity of TiAl alloys to form abundant local ICO order for Al-rich compositions.

Inspired by these results, we performed extensive MD simulations of the patchy-particle model for binary alloys containing atoms with different crystalline symmetries (fcc, bcc, and hcp) and for alloys containing atoms with crystalline symmetries and atoms with ICO symmetries. We find that the minimum R_c does not occur for pure substances. For binary alloys containing atoms with different crystalline symmetries, the minimum R_c is only a factor of ~5 lower than that for pure substances, which is consistent with experimental studies of binary and multicomponent alloys, whose elements readily crystallize. In contrast, R_c for binary alloys containing atoms with ICO and crystalline symmetries can be reduced

by more than three orders of magnitude relative to that for pure substances by increasing the fraction of atoms with ICO symmetry. These results emphasize that the GFA of binary alloys can be greatly increased by including elements that enhance local ICO order. However, R_c for mixtures containing atoms with ICO and crystalline symmetries is not monotonic; we show that R_c possesses a minimum for the ICO-rich systems where quasicrystals can form. In addition, for binary alloys where eutectic points are absent, we find that the GFA is not strongly correlated with the melting curve. We show that these results are consistent with experimental studies of binary, ternary, and multicomponent alloys and EAM MD simulations of NiCu and TiAl.

The remainder of the paper is organized as follows. In Sec. II, we introduce the simulation methods, including the EAM and patchy-paticle interaction potentials, the methods that we use to characterize the crystalline and quasicrystalline order, and quantification of the critical cooling rate. In this section, we also describe the cosputtering and x-ray diffraction experiments that were performed. In Sec. III, we present the main results for the MD simulations of the EAM and patchy-particle interaction potentials and for the experiments on the binary, ternary, and multicomponent alloys. We provide the conclusions in Sec. IV, as well as promising directions for future research. We also include two Appendices to supplement the main text. In Appendix A, we present additional details concerning the structural characterization of sputtered samples using x-ray diffraction and, in Appendix B, we describe the results from EAM MD simulations of CuZr binary alloys.

II. METHODS

We carry out MD simulations of binary alloys (with elements that have similar atomic radii) cooled from the high-temperature liquid state to low temperatures well below the glass transition temperature T_g to measure the critical cooling rate R_c, below which crystallization (or the formation of quasicrystals) occurs. We focus on two models for the atomic interactions: (1) EAM potentials, which include isotropic pairwise interactions and many-body interactions that arise from the electronic degrees of freedom and (2) the effective patchy-particle potential, which includes anisotropic pairwise interactions to stabilize particular crystalline symmetries, e.g., fcc, hcp, and bcc, or systems with local ICO order. We also describe cosputtering deposition and x-ray diffraction experiments to characterize the GFA of several binary, ternary and multicomponent alloys with similar atomic sizes at cooling rates $R \sim 10^9$ K/s.

A. MD simulations of binary alloys using EAM potentials

We first focus on two specific binary alloys with similar atomic radii: NiCu and TiAl. Several key features of the four elements are shown in Table I. The cohesive energies of Ni and Cu differ by 27% and that of Al and Ti differ by 52%, which gives rise to different melting temperatures T_m for the pure substances (see below). The equilibrium crystal structure of Ni and Cu is fcc at room temperature. Al also forms fcc crystals in equilibrium at room temperature, while Ti forms

TABLE I. Several important physical properties of Ni, Cu, Ti, and Al, including the atomic diameter σ, cohesive energy ϵ, melting temperature T_m, and the equilibrium crystal structure at room temperature [14,25].

Element	σ (Å)	ϵ (eV/atom)	T_m (K)	Crystal Structure
Ni	2.52	4.44	1728	fcc
Cu	2.52	3.49	1358	fcc
Ti	2.84	4.85	1941	hcp
Al	2.80	3.39	933.5	fcc

hcp crystals. To model these two alloys, we carry out MD simulations using the EAM potentials developed in Refs. [26,27], which have been validated by comparing structural properties (i.e., the pair correlation function and local atomic order) in crystalline and amorphous states and the GFA to experimental results [28,29]. We show that the atomic radii in these binary alloys are similar by plotting the effective isotropic pairwise contributions $V_{\mathrm{eff}}(r_{ij})$ to the EAM potentials. The minima in $V_{\mathrm{eff}}(r_{ij})$ for the Cu-Cu, Cu-Ni, and Ni-Ni interactions occur near 2.5 Å, and the minima in $V_{\mathrm{eff}}(r_{ij})$ for the Al-Al, Ti-Al, and Ti-Ti interactions occur near 2.8 Å, as shown in Figs. 1(a) and 1(b).

The EAM MD simulations are initialized with $N = 2000$ atoms placed on an fcc lattice. (We also carried out simulations with $N = 8000$ atoms and found similar results for the composition-dependent critical cooling rate.) The initial temperature is $T_0 = 2500$ K, which is much larger than T_m of the pure substances, so the systems melt and reach an equilibrium liquid state. The liquid is then cooled linearly with rate R to 300 K $\ll T_g$ so the system forms a solidlike state. The simulations are performed using periodic boundary conditions in cubic cells and at constant pressure $P = 0$ using the Nose-Hoover barostat with a time step $\Delta t = 0.002$ ps to integrate the equations of motion. 50 independent simulations are performed for each R. After the systems are thermally quenched to low temperature, we characterize the local atomic structure (described in Sec. II C) at each cooling rate.

B. MD simulations of binary alloys using the patchy-particle model

In systems modeled using isotropic pair potentials, such as the Lennard-Jones (LJ) interatomic potential, the low-temperature solids possess significant fcc and hcp crystalline
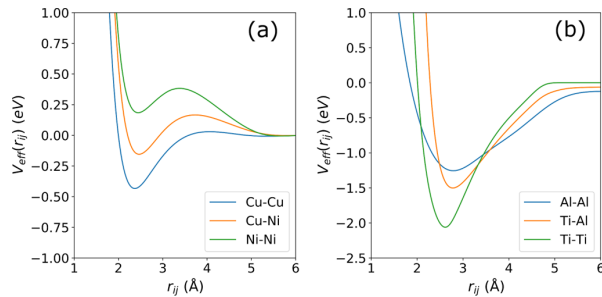

FIG. 1. Effective pairwise interatomic potentials $V_{\mathrm{eff}}(r_{ij})$ for the EAM models of (a) NiCu and (b) TiAl binary alloys.
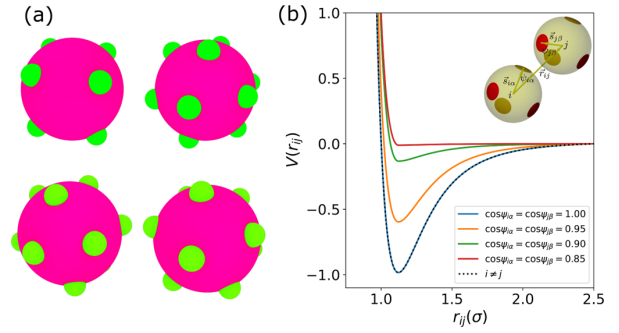

FIG. 2. (a) Examples of patchy particles with different atomic symmetries. The attractive patches (small green spheres) are placed on the surface of the host sphere (large magenta sphere) with bcc (upper left), fcc (upper right), hcp (lower left), and ICO (lower right) symmetries. (b) Patchy-particle pair potentials $V(r_{ij})$ for different values of the preferred angle parameter $\psi_{i\alpha}$, which quantifies the angle between the center-to-center vector $\bar{r}_{ij}$ and the vector $\bar{s}_{i\alpha}$ from the center of sphere i to the center of the αth patch on i. The size of the patch is given by $\delta_{i\alpha}$. Attractive interactions only occur when the two patches α and β on particles i and j (of the same type) face each other as shown in the inset.

order when cooled slowly [15]. However, for binary alloys with similar atomic radii, it is difficult to generate bcc crystalline order using LJ pair potentials. To overcome this difficulty, we use the anisotropic, patchy-particle model [22–24] to generate low-temperature solids with bcc, as well as fcc and hcp order. We can also use the patchy-particle model to enhance local icosohedral order, which encourages glass formation instead of crystallization with long-range order.

In the patchy-particle model, we choose the number and locations of attractive patches that are placed on the surface of each spherical atom to set the preferred local symmetry. For example, to generate fcc symmetry, we can arrange 12 patches on the surface of sphere i, where the center-to-center separation unit vectors $\hat{r}_{ij}$ between sphere i and its nearest neighbors j point to the fcc lattice positions that are on the surface of sphere i. We follow a similar procedure for generating patchy-particles with hcp and bcc symmetries. For icosahedral symmetry, sphere i is placed at the center of an icosahedron and the centers of the patches are placed at the vertices of the icosahedron. The numbers of patches and their placement on spherical atoms are shown in Table II and Fig. 2(a).

The patchy-particle potential is defined by

$$V(r_{ij}) = V_{\mathrm{LJ}}^r(r_{ij}) + V_{\mathrm{LJ}}^a(r_{ij})v(\psi_{i\alpha}, \psi_{j\beta}), \qquad (1)$$

where r_{ij} is the separation between atoms i and j of the same atomic species. The first term $V_{\mathrm{LJ}}^r(r_{ij})$ involves the purely repulsive LJ interaction, which prevents atomic overlaps. The second term involves the attractive part of the LJ potential $V_{\mathrm{LJ}}^a(r_{ij})$, and turns on when patch α on atom i is aligned with patch β on atom j of the same type. $V_{\mathrm{LJ}}^r(r_{ij})$ and $V_{\mathrm{LJ}}^a(r_{ij})$ are

TABLE II. Positions of the centers of patches on the host atom (in units of its radius $\sigma/2$), where the origin is at the center of the host atom. We also define $\phi_0 = \sqrt{\frac{2}{5+\sqrt{5}}}$ and $\phi_1 = \sqrt{\frac{1+\sqrt{5}}{2\sqrt{5}}}$.

#	bcc	fcc	hcp	ICO
1	$\left(\frac{1}{\sqrt{3}}, \frac{1}{\sqrt{3}}, -\frac{1}{\sqrt{3}}\right)$	$\left(\frac{1}{\sqrt{2}}, \frac{1}{\sqrt{2}}, 0\right)$	$(1, 0, 0)$	$(0, \phi_0, \phi_1)$
2	$\left(\frac{1}{\sqrt{3}}, -\frac{1}{\sqrt{3}}, \frac{1}{\sqrt{3}}\right)$	$\left(\frac{1}{\sqrt{2}}, -\frac{1}{\sqrt{2}}, 0\right)$	$(-1, 0, 0)$	$(0, -\phi_0, \phi_1)$
3	$\left(-\frac{1}{\sqrt{3}}, \frac{1}{\sqrt{3}}, \frac{1}{\sqrt{3}}\right)$	$\left(-\frac{1}{\sqrt{2}}, \frac{1}{\sqrt{2}}, 0\right)$	$\left(\frac{1}{2}, \frac{\sqrt{3}}{2}, 0\right)$	$(0, \phi_0, -\phi_1)$
4	$\left(-\frac{1}{\sqrt{3}}, -\frac{1}{\sqrt{3}}, -\frac{1}{\sqrt{3}}\right)$	$\left(-\frac{1}{\sqrt{2}}, -\frac{1}{\sqrt{2}}, 0\right)$	$\left(\frac{1}{2}, -\frac{\sqrt{3}}{2}, 0\right)$	$(0, -\phi_0, -\phi_1)$
5	$\left(-\frac{1}{\sqrt{3}}, -\frac{1}{\sqrt{3}}, \frac{1}{\sqrt{3}}\right)$	$\left(\frac{1}{\sqrt{2}}, 0, \frac{1}{\sqrt{2}}\right)$	$\left(-\frac{1}{2}, \frac{\sqrt{3}}{2}, 0\right)$	$(\phi_1, 0, \phi_0)$
6	$\left(-\frac{1}{\sqrt{3}}, \frac{1}{\sqrt{3}}, -\frac{1}{\sqrt{3}}\right)$	$\left(\frac{1}{\sqrt{2}}, 0, -\frac{1}{\sqrt{2}}\right)$	$\left(-\frac{1}{2}, -\frac{\sqrt{3}}{2}, 0\right)$	$(\phi_1, 0, -\phi_0)$
7	$\left(\frac{1}{\sqrt{3}}, -\frac{1}{\sqrt{3}}, -\frac{1}{\sqrt{3}}\right)$	$\left(-\frac{1}{\sqrt{2}}, 0, \frac{1}{\sqrt{2}}\right)$	$\left(0, \frac{1}{\sqrt{3}}, \sqrt{\frac{2}{3}}\right)$	$(-\phi_1, 0, \phi_0)$
8	$\left(\frac{1}{\sqrt{3}}, \frac{1}{\sqrt{3}}, \frac{1}{\sqrt{3}}\right)$	$\left(-\frac{1}{\sqrt{2}}, 0, -\frac{1}{\sqrt{2}}\right)$	$\left(-\frac{1}{2}, -\frac{\sqrt{3}}{6}, \sqrt{\frac{2}{3}}\right)$	$(-\phi_1, 0, -\phi_0)$
9	–	$\left(0, \frac{1}{\sqrt{2}}, \frac{1}{\sqrt{2}}\right)$	$\left(\frac{1}{2}, -\frac{\sqrt{3}}{6}, \sqrt{\frac{2}{3}}\right)$	$(\phi_0, \phi_1, 0)$
10	–	$\left(0, \frac{1}{\sqrt{2}}, -\frac{1}{\sqrt{2}}\right)$	$\left(0, \frac{1}{\sqrt{3}}, -\sqrt{\frac{2}{3}}\right)$	$(-\phi_0, \phi_1, 0)$
11	–	$\left(0, -\frac{1}{\sqrt{2}}, \frac{1}{\sqrt{2}}\right)$	$\left(-\frac{1}{2}, -\frac{\sqrt{3}}{6}, -\sqrt{\frac{2}{3}}\right)$	$(\phi_0, -\phi_1, 0)$
12	–	$\left(0, -\frac{1}{\sqrt{2}}, -\frac{1}{\sqrt{2}}\right)$	$\left(\frac{1}{2}, -\frac{\sqrt{3}}{6}, -\sqrt{\frac{2}{3}}\right)$	$(-\phi_0, -\phi_1, 0)$

defined using the LJ interaction potential,

$$V_{\mathrm{LJ}}(r_{ij}) = 4\epsilon_{ij}\left[\left(\frac{\sigma}{r_{ij}}\right)^{12} - \left(\frac{\sigma}{r_{ij}}\right)^{6}\right], \qquad (2)$$

where σ is the atomic diameter. In particular, the purely repulsive part $V_{\mathrm{LJ}}^r(r_{ij}) = V_{\mathrm{LJ}}(r_{ij})$ for $r_{ij} < 2^{1/6}\sigma$ and $V_{\mathrm{LJ}}^r(r_{ij}) = 0$ otherwise. In contrast, the attractive part $V_{\mathrm{LJ}}^a(r_{ij}) = 0$ for $r_{ij} < 2^{1/6}\sigma$ and $V_{\mathrm{LJ}}^a(r_{ij}) = V_{\mathrm{LJ}}(r_{ij})$ otherwise.

The angle-dependent attractive interactions are defined using

$$v(\psi_{i\alpha}, \psi_{j\beta}) = \exp\left[-\frac{(1 - \cos\psi_{i\alpha})^2}{\delta_{i\alpha}^2}\right]$$
$$\times \exp\left[-\frac{(1 - \cos\psi_{j\beta})^2}{\delta_{j\beta}^2}\right], \qquad (3)$$

where $\psi_{i\alpha}$ is the angle between the center-to-center separation vector $\vec{r}_{ij}$ from atom i to j and the position vector $\vec{s}_{i\alpha}$ that locates patch α on the surface of atom i and $\delta_{i\alpha}/\sigma = \delta_{j\beta}/\sigma = 0.1$ determines the range of $\psi_{i\alpha}$ values that contribute to the energy, as illustrated in the inset to Fig. 2(b). The attractive interactions are only nonzero when $\vec{r}_{ij}$ is aligned with both of the position vectors that locate patch α on i and patch β on j, i.e., $\psi_{i\alpha} \cong \psi_{j\beta} \cong 0$. [See Fig. 2(b).]

Atoms i and j can be of the same element type or different. The anisotropic interactions are only nonzero between like species, i.e., we set $\psi_{i\alpha} = \psi_{j\beta} = 0$ when i and j are different atom types so different atomic species interact via the isotropic LJ potential. The energetic parameters ϵ_{AA} and ϵ_{BB} give the cohesive energies of the pure substances, and ϵ_{AB} is the interaction energy between atom types A and B ($\epsilon_{AB} = \sqrt{\epsilon_{AA}\epsilon_{BB}}$). The patchy-particle potential $V(r_{ij})$ is truncated and shifted at $r_{ij} = 2.5\sigma$. When calculating the forces between atoms i and j, we only include the pair of patches α and β that maximizes the value of $v(\psi_{i\alpha}, \psi_{j\beta})$.

In this paper, we consider three sets of cohesive energies: (i) the cohesive energy ϵ is the same for atoms with fcc, bcc, hcp, and ICO symmetries; (ii) the cohesive energy ϵ is the same for atoms with fcc, bcc, and ICO symmetries, while $\epsilon_{\mathrm{hcp}} = 2\epsilon$ for atoms with hcp symmetry, which ensures that pure substances with fcc, bcc and hcp symmetries have the same R_c; and (iii) the cohesive energy for atoms with hcp symmetry $\epsilon_{\mathrm{hcp}} = 3\epsilon_{\mathrm{fcc}}$ so the GFA of pure substances with hcp symmetry is worse than that for pure substances with fcc symmetry. By tuning the cohesive energy, we can vary the GFA of the pure substances with fcc, bcc, hcp, and ICO symmetries, as well as the six types of binary mixtures. In this work, we consider binary mixtures containing atoms with (1) hcp and fcc symmetries, (2) hcp and bcc symmetries, and (3) fcc and bcc symmetries, as well as mixtures with (4) hcp and ICO symmetries, (5) bcc and ICO symmetries, and (6) fcc and ICO symmetries.

We simulated $N = 1000$ patchy particles in cubic cells with periodic boundary conditions to measure the critical cooling rate as a function of the fraction of atoms with a given type of symmetry. In our previous work [15], where we carried out computational studies of equal-sized binary LJ alloys, we showed that the critical cooling rate depends only weakly on system size for $N \geqslant 1000$ atoms. We also carried out simulations with $N = 3456$ patchy particles, which gave similar results to those for $N = 1000$. We first equilibrate the system in a liquid state at high temperature well above the melting temperatures of the pure substances. We then cool the system linearly with rate R from high to low temperature $T_f/\epsilon = 0.1$, well below T_g. We integrated the equations of motion using a time step $\Delta t = 0.001$ at constant volume with density $\rho = 1.0$. 20 independent runs are performed at each composition f_B and cooling rate R to generate ensemble averages. The results from the patchy-particle model simulations are reported in reduced units: ϵ_{AA} for energies, σ_{AA} for length scales, and $\sigma_{AA}\sqrt{m/\epsilon_{AA}}$ for timescales. The Boltzmann constant k_B is set to unity.

C. Structure analysis

To determine the critical cooling rate R_c, we analyze the local structural order of the solid-like states obtained by quenching the systems to low temperature. We have two goals: (1) identify the symmetry of the local positional order for each atom and (2) identify the fraction of atoms in the system that possess crystalline (with either fcc, bcc, or hcp symmetry) or quasicrystaline order.

To perform the first task, we define two measures of the local bond-orientational order, Q_l and W_l. We first identify the nearest neighbors of each atom by performing Voronoi tesselation of the atomic centers. We calculate the l-fold symmetric complex bond orientational order parameter $q_{lm}(i)$ for each atom i:

$$q_{lm}(i) = \frac{1}{N_i} \sum_{j=1}^{N_i} \frac{A_j}{A_{\text{tot}}^i} Y_{lm}(\theta(\mathbf{r}_{ij}), \phi(\mathbf{r}_{ij})), \quad (4)$$

where N_i is the number of nearest (Voronoi) neighbors of atom i, m is an integer between $-l$ and l, $Y_{lm}(\theta(\mathbf{r}_{ij}), \phi(\mathbf{r}_{ij}))$ is the spherical harmonic with degree l and order m, and θ and ϕ are the polar and azimuthal angles in a spherical coordinate system centered on atom i. The contribution from the spherical harmonics of each neighbor j of atom i is weighted by the fraction A_j/A_{tot}^i of the area of the Voronoi face separating the two atoms to the total area of all faces A_{tot}^i of the polyhedron surrounding atom i. We calculate the average complex bond orientational order parameter $Q_{lm}(i)$ by averaging $q_{lm}(i)$ over the first coordination shell:

$$Q_{lm}(i) = \frac{1}{N_i + 1} \left(q_{lm}(i) + \sum_{j=1}^{N_i} q_{lm}(j) \right). \quad (5)$$

The real-valued bond-orientational order parameter Q_l is obtained by summing the magnitude squared of $Q_{lm}(i)$ over m:

$$Q_l(i) = \sqrt{\frac{4\pi}{2l+1} \sum_{m=-l}^{l} |Q_{lm}(i)|^2}. \quad (6)$$

Another measure of bond orientational order is calculated using

$$W_l(i) = \sum_{m_1+m_2+m_3=0} \begin{pmatrix} l & l & l \\ m_1 & m_2 & m_3 \end{pmatrix} Q_{lm_1}(i) Q_{lm_2}(i) Q_{lm_3}(i) \quad (7)$$

and

$$\widehat{W}_l(i) = \frac{W_l(i)}{\left(\sum_{m=-l}^{l} |Q_{lm}(i)|^2 \right)^{\frac{3}{2}}}, \quad (8)$$

where $\begin{pmatrix} l & l & l \\ m_1 & m_2 & m_3 \end{pmatrix}$ is the Wigner 3-j symbol. Similar quantities, w_l and $\widehat{w}_l$, which are not averaged over the first coordination shell, can be defined using Eqs. (7) and (8) by replacing $Q_{lm}(i)$ with $q_{lm}(i)$.

The combination of order parameters Q_6, $\widehat{W}_6$, and $\widehat{W}_4$ can be used to identify the symmetry of the local positional order [30]. First, we only consider atoms with a sufficient amount of bond orientational order, i.e., $Q_6 > a$, where $a = 0.25$. bcc-like order satisfies $\widehat{W}_6 > 0$; fcc-like order satisfies $\widehat{W}_6 \leqslant 0$ and $\widehat{W}_4 < 0$; and hcp-like order satisfies $\widehat{W}_6 \leqslant 0$ and

$\widehat{W}_4 > 0$. Atoms with ICO symmetry possess $Q_6 < a$ and $w_6 < -0.023$. Using this method, we can determine the fraction of atoms, c, with fcc, hcp, and bcc positional order, as well as identify those atoms with local icosohedral order.

We now seek to determine the number of crystal- or quasicrystal-like atoms in the system independent of the type of symmetry of the local positional order. To do this, we calculate the order parameter

$$s_l(i, j) = \frac{\sum_{m=-l}^{l} q_{lm}(i) q_{lm}^*(j)}{\sqrt{\sum_{m=-l}^{l} |q_{lm}(i)|^2} \sqrt{\sum_{m=-l}^{l} |q_{lm}(j)|^2}}, \quad (9)$$

where j indicates a Voronoi neighbor of atom i. When $s_l(i, j) \geqslant b_c$, the bond between atoms i and j is considered crystalline or quasicrystalline, otherwise it is considered disordered. In this paper, we find $l = 6$ and $b_c = 0.7$ can effectively detect the formation of crystal structures (fcc, hcp, and bcc) [31], while $l = 12$ and $b_c = 0.45$ can detect the formation of quasicrystalline structures [32]. To detect quasicrystalline structures, we calculate $s_{12}(i, j)$ including neighbors with separations $r_{ij} < 2.31\sigma$ as in Ref. [32]. If more than half the bonds between atom i and its neighbors are crystalline or quasicrystalline, the central atom i is labeled as crystalline or quasicrystalline. Thus, we can calculate the fraction of crystalline and quasicrystalline atoms $f_c = N_c/N$ and $f_q = N_q/N$, where N_c (N_q) is the number of crystalline (quasicrystalline) atoms, as a function of the cooling rate R.

D. Calculation of the critical cooling rate R_c

In prior studies [15], which focused on systems that mainly form fcc crystals at low cooling rates, we calculated $\langle Q_6 \rangle$ as a function of R to determine the critical cooling rate R_c. Atoms with fcc-, hcp-, and bcc-like order possess different values of Q_6, and thus Q_6 alone cannot be used to identify the critical cooling rate. Instead, we calculate the fraction f_c (or f_q) of crystalline (or quasicrystalline) atoms as a function of R. In general, we find that

$$f_{c,q} = \frac{1}{2} \left(1 - \tanh \left[\log_{10} \left(\frac{R}{R_c} \right)^{\frac{1}{\kappa}} \right] \right), \quad (10)$$

where $0 < \kappa < 1$ is the stretching exponent. The critical cooling rate R_c is defined as the rate at which $f_c = 0.5$ (or $f_q = 0.5$).

E. Cosputtering deposition and x-ray diffraction experiments

Compositionally graded alloy libraries were fabricated using confocal dc magnetron cosputtering (AJA International ATC2200), as illustrated in Ref. [33]. The sputtering targets for the TiAl, CrNiCu, and CrFe-CoNi-Cu alloys were loaded into sputtering sources, which were tetrahedrally arranged toward the substrate, pointing at its center at an angle of $29.8°$. Two libraries were prepared for the TiAl binary system, with sputtering powers adjusted on each source to yield approximate center compositions of $Ti_{75}Al_{25}$ and $Ti_{25}Al_{75}$. One library was prepared for the ternary and quinary system each. The sputtering target purities were 99.99% or better (Kurt Lesker Company). Films were deposited to a thickness of 500 nm on 100-mm-diameter silicon wafer substrates with

$3\,\mu$m thermal oxide (University Wafer Inc.). The substrate was masked to yield 3-mm alloy patches on a 6-mm square grid. Before each cosputtering fabrication, the processing chamber was evacuated to a base pressure of 5.0×10^{-7} Torr or less. The films were then deposited by flowing ultrahigh purity argon at 5.8×10^{-3} Torr. Composition distributions were measured using automated energy dispersive x-ray fluorescence spectroscopy (with a Helios G4 UX DualBeam FIB at Yale University's Materials Characterization Core, as well as an Oxford Instruments X-Max detector attached to a Zeiss Sigma VP Field Emission scanning electron microscope at Southern Connecticut State University). For the binary libraries, the composition distribution was measured along the respective line of patches with the widest available composition range. X-ray diffractograms were measured on the same line of patches with a Rigaku Smartlab x-ray diffractometer using Bragg-Brentano focusing, Cu-Kα radiation, and a 2-mm beam mask. For the ternary and quinary library systems, diffractograms were measured using high-throughput x-ray diffraction at the Stanford Synchrotron Radiation Lightsource at SLAC National Accelerator Laboratory, beamline 1–5. The photon energy was 12.7 keV. The composition range of glass formation and crystal structures were determined from the resulting diffractograms. (See Appendix A.)

III. RESULTS

In this section, we describe the results for the GFA of binary alloys modelled using both the EAM and patchy-particle potentials, as well as the results for the sputtering and x-ray diffraction experiments on binary, ternary, and multicomponent alloys, all with similar atomic sizes. For the EAM MD simulations, we calculate the critical cooling rates for NiCu and TiAl binary alloys and show that the composition-dependent R_c is very different for these two alloys systems. In contrast to the NiCu alloys, the TiAl alloys can possess strong local ICO order, leading to significantly lower critical cooling rates. To investigate the effect of each element's atomic symmetry on the GFA of binary alloys, we carried out extensive MD simulations of the patchy-particle model including mixtures of atoms with crystalline and local ICO symmetries. We find that the critical cooling rate decreases strongly when the alloys contain elements with ICO symmetry. However, the dependence of R_c on local ICO order is not monotonic with the fraction of atoms with icosahedral symmetry f_{ICO}; when $f_{\mathrm{ICO}} > 0.8$, quasicrystals form, which causes R_c to increase. We also show that for systems where there are no eutectics in the equilibrium phase diagram for an alloy, the GFA and effective melting curve are not strongly correlated. These results for the GFA for the patchy-particle model are consistent with EAM MD simulations of binary alloys and experiments on binary, ternary, and multicomponent alloys containing elements with similar atomic sizes.

A. GFA of binary alloys using EAM MD simulations

We first investigate the GFA of two specific binary alloys, NiCu and TiAl, both with similar atomic sizes, using MD simulations of the EAM potentials to determine R_c versus the alloy composition [26,27]. In Fig. 3, we show results
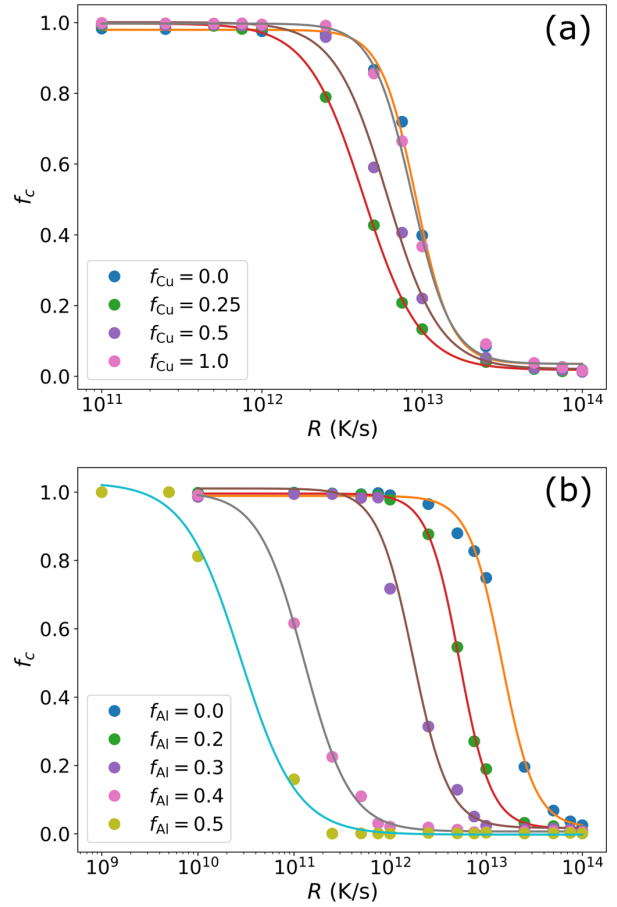

FIG. 3. The fraction of crystalline atoms f_c as a function of cooling rate R from EAM MD simulations of (a) NiCu (for several values of the fraction of Cu atoms f_{Cu}) and (b) TiAl (for several values of the fraction of Al atoms f_{Al}). The solid lines give fits to Eq. (10).

for the fraction f_c of atoms in crystalline environments as a function of cooling rate R for NiCu and TiAl alloys. In general, f_c versus $\log_{10} R$ is sigmoidal, $f_c \sim 1$ for low cooling rates, $f_c \sim 0$ for high cooling rates, and the R_c is determined by $f_c(R_c) = 0.5$. For the NiCu binary alloys, $R_c \sim 10^{12}$-10^{13} K/s and only depends weakly on the composition. In contrast, R_c depends strongly on the fraction of Al atoms in TiAl alloys, ranging from $\sim 10^{13}$ K/s for pure Ti to 10^{10} K/s for $\mathrm{Al}_{50}\mathrm{Ti}_{50}$. In Fig. 4(a), we show that R_c for NiCu alloys varies by less than a factor of 5 over the full range of composition. In contrast, R_c for TiAl decreases strongly as f_{Al} increases away from pure Ti. When f_{Al} is increased above 0.5, quasicrystals form before the alloys form their equilibrium crystalline phases. Thus, in the range $0.5 < f_{\mathrm{Al}} < 1.0$, we determine R_c according to $f_q(R_c) = 0.5$, where f_q is the fraction of atoms in quasicrystalline local environments.

To validate the critical cooling rate R_c data from the EAM MD simulations, one needs experimental data on the atomic structure over a wide range of cooling rates for each composition in each binary alloy. However, experimental
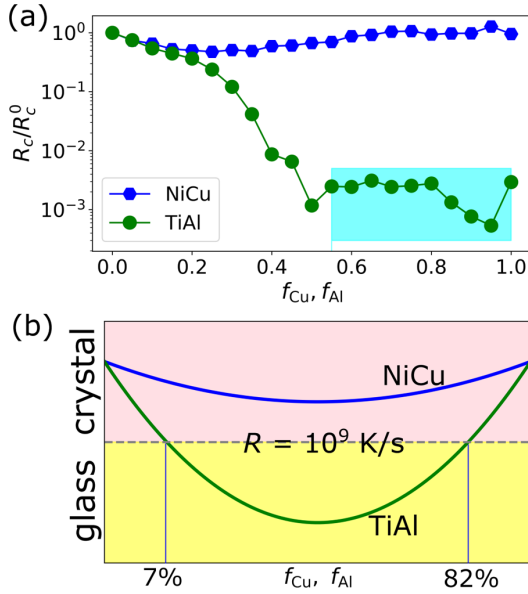
FIG. 4. (a) The critical cooling rate R_c/R_c^0 for NiCu (normalized by R_c^0 for pure Ni) versus the fraction f_{Cu} of Cu atoms, and TiAl (normalized by R_c^0 for pure Ti) versus the fraction f_{Al} of Al atoms, obtained using EAM simulations. The binary alloys with $f_{Al} \gtrsim 0.5$ (cyan region) form quasicrystals for $R < R_c$. (b) Schematic diagram of solidification for NiCu and TiAl alloys based on cosputtering experiments, which correspond to $R \sim 10^9$ K/s. NiCu alloys crystallize over the full range of f_{Cu}, while TiAl alloys form glasses for $0.07 < f_{Al} < 0.82$.

studies using state-of-the-art cosputtering methods currently only measure the atomic structure at one cooling rate ($\sim 10^9$ K/s) over the full range of compositions. Thus, these experimental studies can only determine whether each composition is crystalline or amorphous at the single cooling rate, $R = 10^9$ K/s. We encourage future experimental studies that measure the atomic structure of alloys over a wide range of cooling rates.

As discussed in Sec. II E, we performed cosputtering and x-ray diffraction studies of the binary alloys NiCu and TiAl. For the NiCu binary alloys, we found that all of the compositions were crystalline. The EAM MD simulations for NiCu are consistent with these experimental results in the sense that $R_c \gtrsim 10^{13}$ K/s is large (compared to that for TiAl) and only weakly dependent on the Cu fraction. [See Fig. 4(b).] In the experimental studies of TiAl, the compositions near pure Ti (<8% Al) and near pure Al >82% Al) are crystalline, but the remaining compositions are amorphous. (See the corresponding x-ray diffractograms in Appendix A.) In the EAM simulations of TiAl, we find that R_c drops rapidly as a function of increasing Al fraction and then R_c begins increasing for large Al fraction. Although the experimental R_c data is not quantitatively the same as the MD simulation data, both sets of data show that R_c is nonmonotonic as a function of the Al fraction and R_c can be much lower for TiAl than CuNi. These results from the EAM MD simulations and experiments serve

to motivate our simulations of binary alloys with different atomic symmetries using the patchy-particle model.

Although Al crystallizes into fcc structures in equilibrium, experimental studies have shown that Al-based metallic glasses possess local ICO order centered on the Al atoms and may form metastable quasicrystals [34–36]. In addition, EAM MD simulations have shown that pure Al forms quasicrystals by rapid quenching [21,37]. In previous studies, Sheng *et al.* characterized the structural properties of a wide range of Al-based metallic glasses using EAM MD simulations [38] and found that the average coordination number can vary from 10 to 20 as a function of the size ratio of the atomic species. In binary metallic glasses, when the atomic sizes of Al and the other element are similar, Sheng *et al.* found that the coordination number is ~ 12, which is consistent with local ICO order. The above results for TiAl and other Al-based binary alloys suggest that mixtures of elements with crystalline and ICO atomic symmetries, *and similar atomic sizes*, can yield alloys with R_c that are several orders of magnitude lower than that for pure systems.

In the present paper, we carried out EAM MD simulations of binary alloys composed of elements with the same atomic sizes, such as Al and Ti (and Ni and Cu). In binary alloys with the same atomic sizes, we argue that the cohesive energy and atomic symmetry are dominant features in determining the GFA. In future studies, we will carry out EAM MD simulations of binary alloys composed of Ni, Fe, Co, and Cu (all with similar atomic sizes), as well as binary alloys composed of Al, Ti, Zn, Mo, Pd, Te, Pt, and Au (all with similar atomic sizes), to generalize the results we found. If we consider binary alloys with different atomic sizes, this feature can compete with the other features—the cohesive energy and atomic symmetry——and change the results for the GFA found for binary alloys composed of elements with similar sizes. In future studies, we will also consider how all three features (cohesive energy, atomic symmetry, and atomic size) affect the GFA of binary alloys.

B. GFA of binary alloys using MD simulations of the patchy-particle model

A limitation of EAM potentials [13] is that the atomic symmetry of the elements cannot be tuned independently, while keeping other important features, such as atomic size and cohesive energy, fixed. To overcome this limitation, we perform MD simulations of the patchy-particle model [24] for binary alloys, where small patches on the surfaces of the same types of atoms attract each other only when they are aligned (and atoms of different types interact via the isotropic LJ potential). Using the patchy-particle model, we study the GFA of binary mixtures of the same-sized atoms with different atomic symmetries (e.g., bcc, fcc, and hcp). Systems that contain atoms with a given symmetry crystallize with that particular symmetry at low cooling rates. In addition, we study mixtures of atoms with crystalline and ICO symmetries by controlling the number and placement of patches on the atom surfaces, which allows us to model a binary alloy in which one element has much better GFA than the other even though both elements have the same atomic sizes.
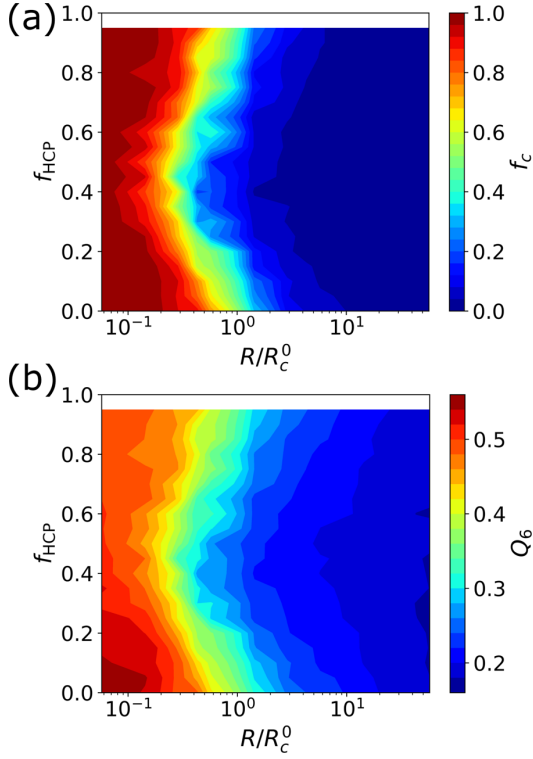
FIG. 5. Contour plots of (a) the fraction of crystalline atoms f_c and (b) the average bond-orientational order parameter $Q_6 = N^{-1}\sum_{i=1}^{N} Q_6(i)$ as a function of the fraction f_{hcp} of atoms with hcp symmetry and the reduced cooling rate R/R_c^0 for MD simulations of the patchy-particle model for binary alloys containing mixtures of atoms with hcp and fcc symmetries. R_c^0 is the critical cooling rate of the pure substance with fcc symmetry. The cohesive energies for the pure substances satisfy $\epsilon_{\mathrm{hcp}} = 2\epsilon_{\mathrm{fcc}}$.

In Figs. 5(a) and 5(b), we show contour plots of the fraction f_c of crystalline atoms and the average bond orientational order parameter $Q_6 = N^{-1}\sum_{i=1}^{N} Q_6(i)$ as a function of the fraction f_{hcp} of atoms with hcp symmetry and cooling rate R from MD simulations of binary alloys modelled as patchy particles with hcp and fcc symmetries. (We chose the cohesive energies for the pure substances, such that $\epsilon_{\mathrm{hcp}} = 2\epsilon_{\mathrm{fcc}}$.) We find that all of the systems crystallize at low R but they form crystals with different symmetries as indicated by the different values of Q_6 for $f_{\mathrm{hcp}} = 0$ and 1. For $f_{\mathrm{hcp}} = 0$, $Q_6 \sim 0.575$, indicating crystallization into fcc crystals. For $f_{\mathrm{hcp}} = 1$, $Q_6 \sim 0.485$, indicating crystallization into hcp crystals. We find similar behavior for the contour plots of f_c and Q_6 versus R/R_c for the other binary mixtures of atoms with crystalline symmetries.

In Fig. 6, we show R_c for binary alloys using the patchy-particle model. In Fig. 6(a), we consider three binary alloys with fcc-bcc, fcc-hcp, and hcp-bcc symmetries for elements *A*-*B* and the same cohesive energies $\epsilon_{AA} = \epsilon_{BB}$. Pure substances with hcp symmetry have the lowest R_c, while R_c is similar for pure substances with fcc and bcc symmetries. In general, we find that R_c is minimal for nonpure substances.

For fcc-bcc binary alloys, the composition with the best GFA has $f_B \approx 0.5$. In contrast, for binary alloys containing atoms with hcp symmetry, the system with minimum R_c has a majority of hcp atoms.

In Fig. 6(b), we plot R_c for binary alloys containing atoms that have fcc, bcc, and hcp symmetries, but the pure substances have similar GFAs (by varying the cohesive energies). As in Fig. 6(a), R_c possesses a minimum in the range $0 < f_B < 1$. For binary alloys containing atoms with bcc symmetry, the system with the lowest R_c has a majority of bcc atoms. For binary alloys with atoms with fcc and hcp symmetries, $f_B \approx 0.5$ has the best GFA since fcc and hcp crystal structures are similar.

In Fig. 6(c), we show R_c for binary alloys containing atoms with fcc and hcp symmetries versus the hcp-fraction f_{hcp}, for three cases where hcp crystals have different GFAs (by adjusting $\epsilon_{\mathrm{hcp}}/\epsilon_{\mathrm{fcc}}$). We find that as R_c at $f_{\mathrm{hcp}} = 1$ decreases, f_{hcp} with the best GFA increases. These results emphasize that the location of the minimum in R_c is influenced by the GFA of the pure substances, which depends on their atomic symmetry and cohesive energy.

As shown in Fig. 6, for binary alloys containing same-sized atoms, but different crystalline symmetries, the minimum R_c changes by only a factor of 5 relative to that for the pure substances. For binary alloys with elements of the same atomic sizes *and* symmetries, we showed previously that R_c scales with the ratio of the cohesive energies of the pure substances [15,24]. Thus, results for R_c for the patchy-particle model are in general agreement with those for EAM simulations of NiCu (with $\epsilon_{\mathrm{Ni}}/\epsilon_{\mathrm{Cu}} \approx 1.3$) in Fig. 4(a), as well as experimental studies of mixtures of Ar and Kr (with $\epsilon_{\mathrm{Kr}}/\epsilon_{\mathrm{Ar}} \approx 1.45$) [39].

Motivated by the results for EAM MD simulations of TiAl in Fig. 4(a), we show R_c for binary alloys containing atoms with ICO and different crystalline symmetries in Fig. 6(d). R_c decreases modestly (by less than an order of magnitude) for $f_{\mathrm{ICO}} \lesssim 0.5$, and decreases dramatically (by more than two orders of magnitude) for $0.5 \lesssim f_{\mathrm{ICO}} \lesssim 0.8$. When $f_{\mathrm{ICO}} \gtrsim 0.8$, the system can form quasicrystals [31], which causes R_c to increase as $f_{\mathrm{ICO}} \to 1$. Note that R_c for elements with ICO symmetry is much lower than that for elements with crystalline symmetry. We find that $R_c(f_{\mathrm{ICO}})$ possesses a minimum near $f_{\mathrm{ICO}} \sim 0.8$. The nonmonotonic behavior of $R_c(f_{\mathrm{ICO}})$ can be rationalized by considering the interfacial free energy barrier for crystal nucleation [31,40–42]. In the crystal-forming regime with $f_{\mathrm{ICO}} \lesssim 0.8$, local ICO order is incompatible with crystalline symmetry, and thus increasing f_{ICO} enhances the free energy barrier for crystal nucleation, leading to decreases in R_c. However, for $f_{\mathrm{ICO}} \gtrsim 0.8$, ICO symmetry becomes compatible with quasicrystalline order, reducing the interfacial free energy barrier and increasing R_c.

C. Decoupling of the critical cooling rate and melting temperature

Prior studies have suggested that in some alloys the composition with the best GFA corresponds to the composition at which the deepest eutectic point occurs on the equilibrium liquidus curve [17,43]. However, many alloys do not possess eutectic points, and there are numerous examples where the best GFA composition deviates from the deepest eutectic point
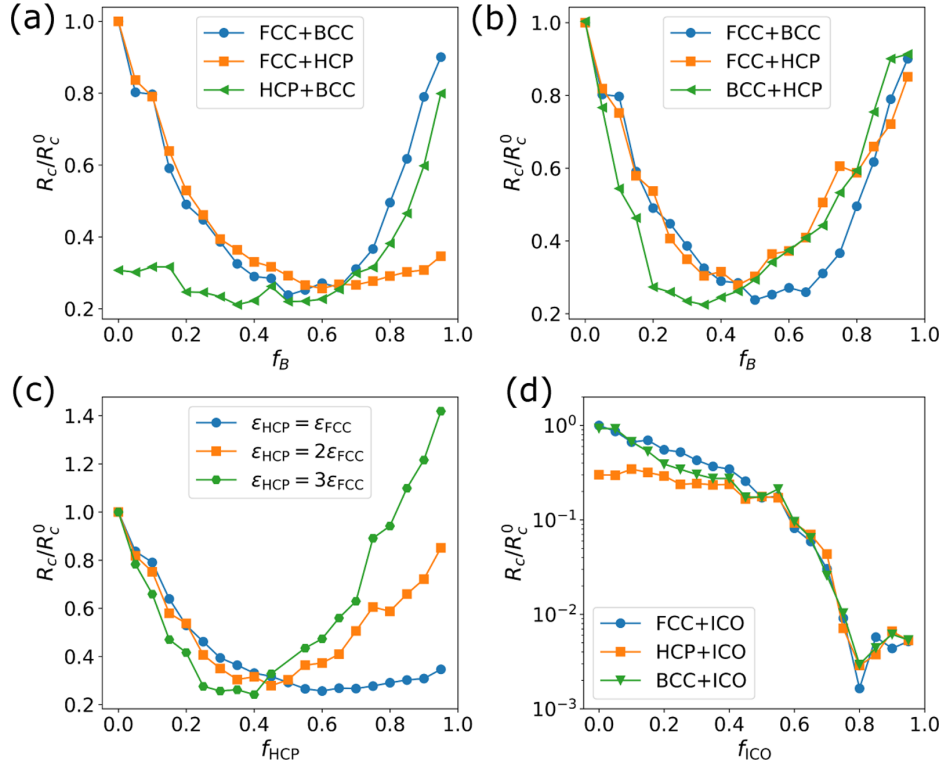
FIG. 6. R_c for binary alloys (normalized by R_c^0 for the pure system with fcc symmetry) using the patchy-particle model. (a) R_c/R_c^0 for binary mixtures with A and B atoms [(A: fcc, B: bcc; circles), (A: fcc, B: hcp; squares), and (A: hcp, B: bcc; triangles)] versus the fraction of B atoms f_B with $\epsilon_{bcc}/\epsilon_{fcc} = \epsilon_{hcp}/\epsilon_{fcc} = 1.0$. (b) R_c/R_c^0 for binary mixtures, where the pure substances (with fcc, bcc, or hcp symmetries) have similar R_c. We set $\epsilon_{bcc}/\epsilon_{fcc} = 1.0$ and $\epsilon_{hcp}/\epsilon_{fcc} = 2.0$. (c) R_c/R_c^0 for binary mixtures with fcc and hcp symmetries, and $\epsilon_{hcp}/\epsilon_{fcc} = 1.0$, 2.0, and 3.0. (d) R_c/R_c^0 for binary mixtures of atoms with crystalline and icosahedral symmetries and the same cohesive energies.

[4,44,45]. To test this point, we measured the effective melting temperature T_m^{eff} (similar to the equilibrium melting temperature T_m, see below) for all of the binary mixtures studied in Fig. 6 and the EAM models of NiCu and TiAl. For cases where the equilibrium crystal structure is known, T_m can be accurately measured by identifying solid-liquid coexistence. However, in our studies, we consider hundreds of binary alloys at different compositions containing atoms with different cohesive energies and atomic symmetries. For most of these alloys, the equilibrium crystal structure is not known. Thus, we use an alternative method for determining the effective melting temperature discussed in Ref. [46], which investigated crystallization and glass formation in MD simulations of binary and ternary alloys using many-body interaction potentials. Specifically, we first crystallize each binary alloy by cooling the system from the liquid state to low temperature using the lowest accessible cooling rate for the simulations. Since this cooling rate is typically much lower than the critical cooling rate, the system crystallizes. We then slowly heat the crystallized sample. During the heating process, we observe a melting transition, which is indicated by a discontinuous jump in the total potential energy per atom V. We show two examples for $V(T)$ in Figs. 7(a) and 7(b) for EAM MD simulations of TiAl at $f_{Al} = 0.5$ and MD simulations of the patchy-particle model for binary mixtures of atoms with fcc and hcp symmetries at $f_{hcp} = 0.5$. Since we generate the

crystallized state using a finite cooling rate and finite system size, the crystal structure typically contains multiple crystalline domains and defects. Thus, we carry out at least 50 independent simulations to calculate the ensemble-averaged melting temperature. Since the elevated cooling rates can generate metastable low-temperature states and the rapid heating rates can induce overheating, we refer to our measurements as the effective melting temperature T_m^{eff}. Despite this, the composition-dependent effective melting temperatures measured for both NiCu and TiAl using this technique are similar to the equilibrium melting curves obtained from experimental studies.

In Fig. 8(a), we show T_m^{eff} for binary alloys containing atoms with different crystalline symmetries, where the pure substances have the same GFA. From experimental data in Fig. 8(c), T_m for pure substances scales roughly linearly with the cohesive energy, although the atomic symmetry gives rise to deviations [25,47]. Thus, T_m for binary alloys containing atoms with different crystalline symmetries is roughly linear in f_B, and the sign of the slope is determined by the sign of $\epsilon_{BB} - \epsilon_{AA}$. We contrast this behavior for $T_m^{eff}(f_B)$ with that for $R_c(f_B)$, which possesses a minimum in the range $0 < f_B < 1$. In Fig. 8(b), we show T_m^{eff} for binary alloys containing atoms with ICO and crystalline symmetries. In this case, T_m^{eff} is nearly constant for $f_{ICO} \gtrsim 0.5$, whereas R_c decreases by more than two orders of magnitude. Thus, we do not find a strong
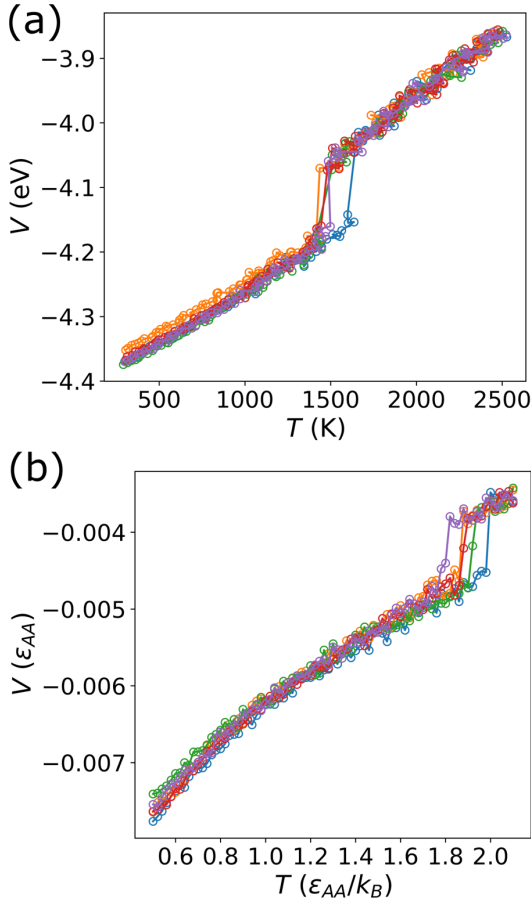
FIG. 7. The potential energy per atom V versus temperature T during heating of low-temperature solids for (a) EAM MD simulations of TiAl at $f_{Al} = 0.5$ and (b) patchy-particle MD simulations of binary mixtures of atoms with hcp and fcc symmetries at $f_{hcp} = 0.5$. For (a), we find $T_m^{eff} \approx 1490 \pm 55$ K using heating rate $R = 10^{10}$ K/s and for (b), we find $T_m^{eff}/(\epsilon_{AA}/k_B) \approx 1.88 \pm 0.08$ using heating rate $R \sim R_c^0$. Five independent simulations are shown for each system. The cohesive energies for the pure substances of the patchy-particle systems satisfy $\epsilon_{hcp} = 2\epsilon_{fcc}$.

correlation between T_m^{eff} (or T_m) and GFA in the binary alloys with the same atomic sizes, but difference cohesive energies and atomics symmetries, that we consider.

To what extent are the results for the patchy-particle model consistent with those for the EAM MD simulations of NiCu and TiAl? First, in Figs. 9(a) and 9(c), we show T_m^{eff} versus f_{Cu} for NiCu and versus f_{Al} for TiAl alloys, which are consistent with the experimental melting curves [48]. For NiCu, T_m^{eff} decreases roughly linearly from $\sim$1700 K to $\sim$1400 K over the range $0 < f_{Cu} < 1$. In contrast, $R_c(f_{Cu})$ for NiCu possesses a shallow minimum near $f_{Cu} \sim 0.25$. For TiAl, T_m^{eff} has a small maximum at $\sim$1800 K for $f_{Al} \sim 0.3$, and then T_m^{eff} decreases monotonically for $f_{Al} \gtrsim 0.3$. In contrast, $R_c(f_{Al})$ decreases over the range $0 < f_{Al} < 0.5$ and has a minimum for $f_{Al} \sim 0.9$-0.95 (although the precise location of the minimum is affected by the degree of quasicrystalline

order). These results further emphasize the decoupling of T_m^{eff} (or T_m) and R_c. Importantly, as shown in Figs. 9(b) for NiCu and 9(d) for TiAl, the composition region with the best GFA is the same as that with the largest fraction of atoms with ICO order, and a minimal amount of (fcc, hcp, and bcc) crystalline order.

D. Data collapse of critical cooling rate versus local icosahedral order

Several studies have characterized the local structural order, such as the size and shape of Voronoi polyhedra, local bond orientational order, and changes of nearest neighbor atoms, in glass-forming materials as they are cooled [13]. In particular, researchers have found that the number of atoms with local ICO order increases when good glass-formers are cooled toward the glass transition [49]. Thus, one suggestion for improving the GFA is to maximize the local ICO order. In Fig. 10, we show that R_c for all of the patchy-particle systems studied collapses when plotted against the fraction c_{ICO} of atoms in the system that have local ICO order, where the icosohedral order is characterized using rapid quenches $R > R_c$ for which all of the systems remain disordered. (Note that c_{ICO} is determined by the fraction of atoms that possess $Q_6 < 0.25$ and $w_6 < -0.023$, as discussed in Sec. II C, and should not be confused with f_{ICO}, which is the fraction of atoms with 12 patches arranged with ICO symmetry.) $R_c(c_{ICO})$ has several key features. First, for $c_{ICO} \lesssim 0.06$, where most of the data for the binary mixtures containing atoms with crystalline symmetries exists, R_c decays exponentially with increasing c_{ICO}. In the regime $0.06 \lesssim c_{ICO} \lesssim 0.075$, R_c decreases more rapidly. For $c_{ICO} \gtrsim 0.075$, since the system can form quasicrystals, R_c begins to increase. Thus, we predict nonmonotonic behavior in $R_c(c_{ICO})$.

E. Experimental measurements of the GFA for multicomponent alloys

Additional results from the sputtering and x-ray diffraction experiments [33] on multcomponent alloys with same-sized atoms provide further support for our simulation findings. (See Appendix A for more details concerning the structural characterization of the alloys.) As shown in Fig. 11(a), all compositions for NiCuCr (and NiCu) alloys crystallize for $R \sim 10^9$ K/s. These results emphasize that the atomic symmetry feature for Ni and Cu is fcc and bcc for Cr. The critical cooling rate is large, $R_c > 10^9$ K/s, for all compositions in the alloy system CrNiCu. The results in Fig. 11(b) show that CrFe, CoNi, and Cu do not possess significant ICO atomic symmetry, since there are no amorphous states over the full range of compositions. These experimental results are also consistent with the MD simulation results for the patchy-particle and EAM potentials. The propensity of the elements in CrFe-CoNi-Cu alloys for forming local ICO order is low, and thus these alloys crystallize over the full range of compositions at $R = 10^9$ K/s. These alloys possess worse GFAs than that for TiAl alloys over a wide range of compositions.

IV. CONCLUSIONS

In summary, we employed MD simulations of EAM potentials and the patchy-particle model to investigate the influence
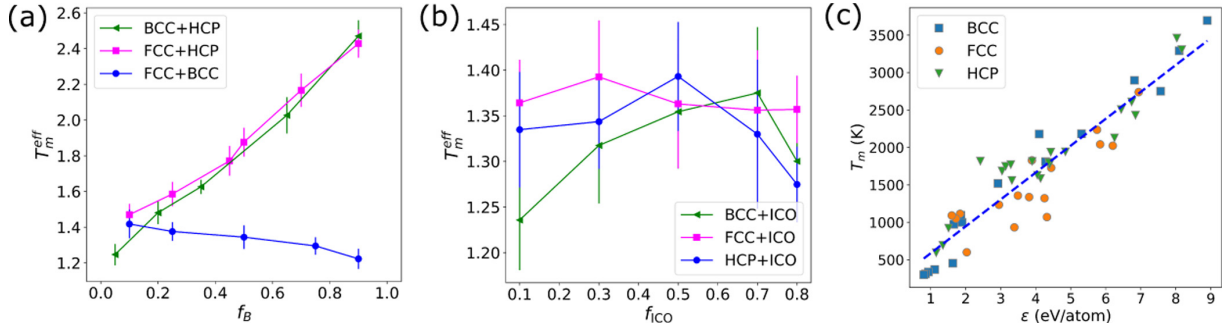
FIG. 8. (a) Effective melting temperature T_m^{eff} for binary alloys (in units of ϵ_{AA}/k_B) using the patchy-particle model for mixtures of A and B atoms. The pure substances have similar R_c; see Fig. 6 (b). (b) T_m^{eff} for binary mixtures of atoms with crystalline and ICO symmetries. T_m^{eff} in (a) and (b) are obtained by heating the quenched crystalline solids to high temperature at rates $R_h \sim R_c^0$. (c) T_m versus the cohesive energy per particle ϵ for 53 pure metals with bcc, fcc, and hcp symmetries in their equilibrium solid forms. The blue dashed line gives $T_m = 0.03\epsilon/k_B$, where k_B is the Boltzmann constant.

of atomic symmetry on the GFA of binary alloys with no atomic size differences. In general, we find that the minimum R_c does not occur for pure substances. For binary alloys containing atoms with different crystalline symmetries, the minimum R_c is only a factor of 5 lower than that for pure substances, which is consistent with recent experimental studies of binary systems, such as NiCu and ArKr, whose elements readily form fcc structures. In contrast, R_c for binary alloys containing atoms with ICO and crystalline symmetries can be reduced by three orders of magnitude relative to that for pure substances by increasing f_{ICO}. These results emphasize

that the GFA of binary alloys can be greatly increased by mixing elements that enhance local ICO order c_{ICO}. However, $R_c(c_{\text{ICO}})$ is not monotonic; we show that R_c possesses a minimum at a characteristic $c_{\text{ICO}} \gtrsim 0.075$, where quasicrystals form. This result may explain why it is difficult to obtain binary BMGs with large amounts of Al (since it may lead to the formation of quasicrystals), whereas minor alloying with Al can dramatically increase the GFA.

We note that our results for binary alloys with similar sized atoms cannot be generalized to binary and ternary alloys with significant atomic size differences. Future EAM and
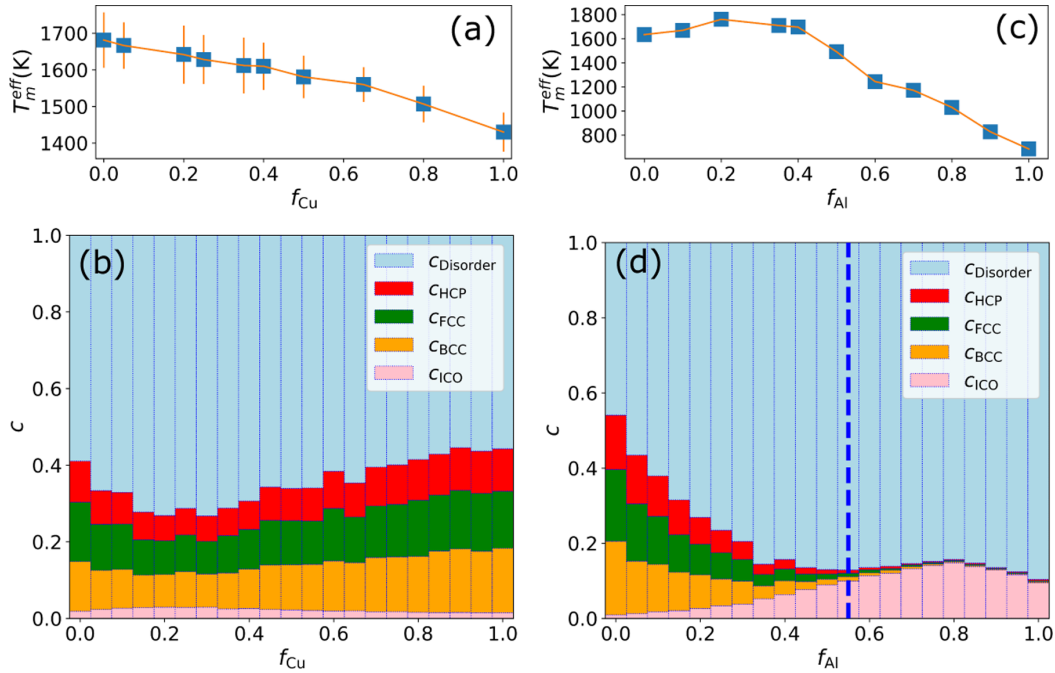

FIG. 9. (a) T_m^{eff} versus f_{Cu} for EAM MD simulations of NiCu using $R_h = 10^{11}$ K/s. (b) Fraction of atoms, c, with a given local order: hcp, fcc, bcc, ICO, or other disordered motifs versus f_{Cu} for zero-temperature systems at $R > R_c$. (c) T_m^{eff} versus f_{Al} for EAM simulations of TiAl using $R_h = 10^{10}$ K/s. (d) Fraction of atoms, c, with a given local order: hcp, fcc, bcc, ICO, and other disordered motifs versus f_{Al} at $R > R_c$. For $f_{\text{Al}} > 0.5$ (vertical dashed line), quasicrystals form for $R < R_c$. The local order in (b) and (d) is measured at $R \sim 10^{13}$ K/s.
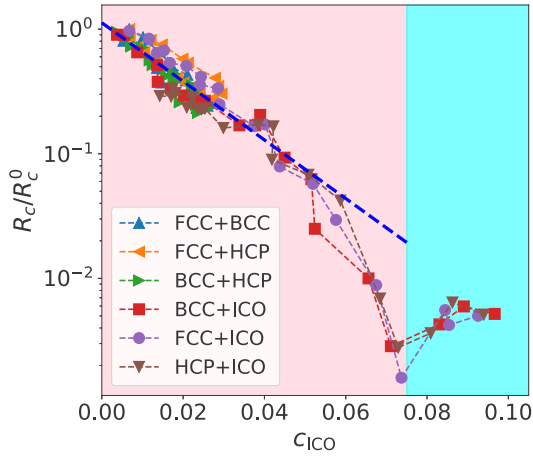
FIG. 10. R_c normalized by R_c^0 for pure substances with fcc symmetry plotted versus the fraction of atoms c_{ICO} with local icosahedral order in binary alloys using the patchy-particle model. c_{ICO} is measured at zero temperature using the lowest R at which all systems remain disordered. For $c_{ICO} \lesssim 0.075$, fcc, bcc, and hcp structures form for $R < R_c$. In the cyan region, systems form quasicrystals for $R < R_c$. The blue dashed line indicates exponential decay, $R_c/R_c^0 \sim \exp(-23.5 c_{ICO})$.

patchy-particle model simulations should consider binary and ternary alloys with cohesive energy, atomic symmetry, and atomic size differences to make comparisons to a broad range of experimental measurements of the critical cooling rates in binary and ternary alloys. But the current findings could provide insights into the GFA of alloys with elements of different sizes. For example, for CuZr, the cohesive energies satisfy $\epsilon_{Zr} > \epsilon_{Cu}$, and thus pure Cu (with fcc symmetry) is expected to have better GFA than pure Zr (with hcp symmetry). (This result is confirmed by EAM MD simulations described in Appendix B, which calculate the R_c of the pure metals). Fur-
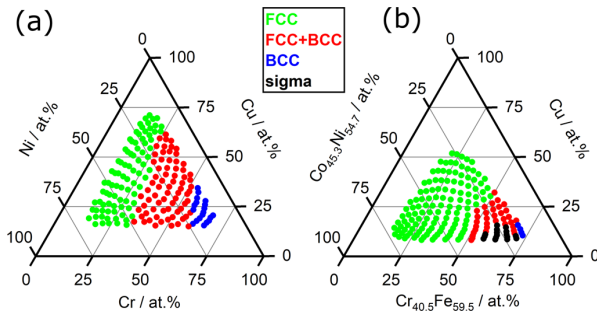

FIG. 11. Crystallization of sputtered (a) CrNiCu and (b) CrFe-CoNi-Cu alloys generated at cooling rate $R \sim 10^9$ K/s. In (a), systems along the binary NiCu axis form fcc crystals, in agreement with the pure substances. With increasing fraction of Cr (with bcc symmetry), the structure transitions to bcc. Crystal formation over the full composition range indicates that $R_c > 10^9$ K/s for all Cr-NiCu (and NiCu) alloys in experiments. Similarly, in (b), we find crystal formation over the full range of compositions in CrFe-CoNi-Cu alloys [33], despite several competing crystalline phases.
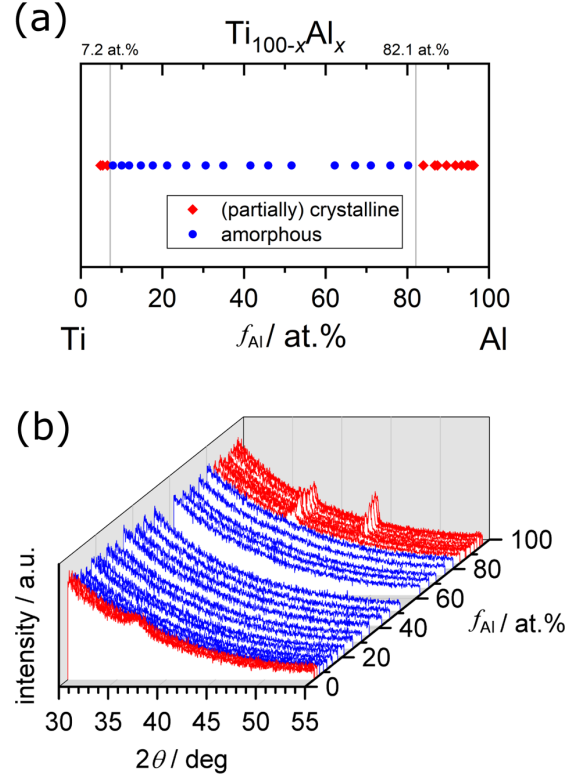

FIG. 12. (a) Composition-structure diagram for all of the TiAl compositions studied. Each marker represents an alloy with an associated fraction of Al atoms, f_{Al}, and a structural classification as either amorphous (blue) or (partially) crystalline (red). Fully amorphous structure is found over the range from $f_{Al} = 0.07$ to 0.82. (b) X-ray diffractograms corresponding to the markers in (a) are arranged along the z axis, which represents the associated binary composition f_{Al}. Based on these diffractograms, an alloy is either classified as amorphous (blue) if no Bragg peaks are observed, or (partially) crystalline (red) otherwise. Diffractograms were acquired for 2θ ranging from 20 to 90°, but are shown over a smaller range here.

ther, Zr is larger than Cu with diameter ratio, $\sigma_{Cu}/\sigma_{Zr} = 0.8$, and based on our prior studies of binary LJ systems [50], Cu-rich alloys (with a majority of smaller atoms) have better GFAs. Thus, based on the cohesive energies and atomic sizes of Cu and Zr, the composition with the best GFA should be Cu rich.

Previous experimental studies of CuZr binary alloys have identified three compositions, $Cu_{64}Zr_{36}$, $Cu_{56}Zr_{44}$, and $Cu_{50}Zr_{50}$, with good GFAs [51]. They showed that the GFAs for $Cu_{64}Zr_{36}$ and $Cu_{50}Zr_{50}$ were comparable within experimental error, and $Cu_{56}Zr_{44}$ had worse GFA than the other two. Experiments by Altounian *et al.* [52] also characterized crystallization and glass formation in CuZr binary alloys over a wide range of compositions. They found that $Cu_{64}Zr_{36}$ possessed the largest activation energy barrier for crystallization. In addition, EAM MD simulations of CuZr binary alloys have shown that $Cu_{64}Zr_{36}$ is the composition with the best GFA, and at this composition the local icosahedral order is
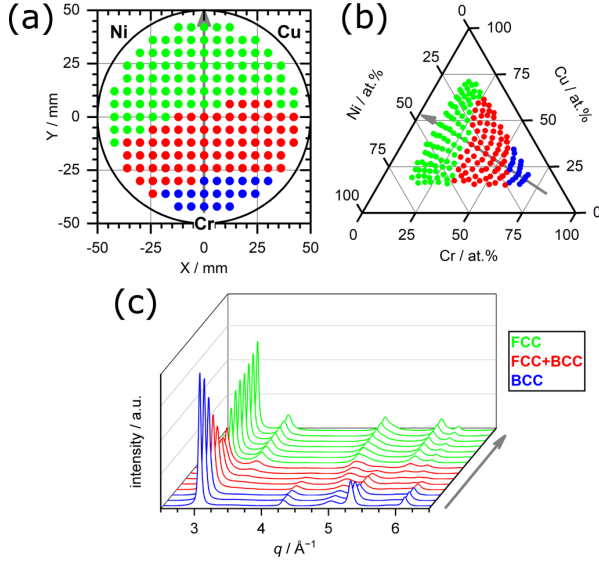
FIG. 13. Experimental data for the as-sputtered Cr-Cu-Ni ternary system. Panels (a) and (b) show the structural classification of each alloy as either bcc, bcc+fcc, or fcc crystal structure. (a) presents a top view of the wafer library. (b) also shows the ternary compositional distribution of these alloys presented as a Gibbs triangle. In (c), a representative selection of x-ray diffractograms is shown. These diffractograms correspond to the line of alloy patches on the Cr-Cu-Ni alloy library that is indicated by the grey arrow in the top panels. All diffractograms here exhibit full crystallinity and are classified as either bcc, bcc+fcc (two-phase region), or fcc structure. (The peak observed at $q \sim 5\,\text{Å}^{-1}$ originates from the substrate's background signal, not the alloys themselves.)

maximum [53]. (See Appendix B.) Thus, consistent with our expectations, these results suggest that the CuZr composition with the best GFA is Cu-rich. In future studies, we will perform MD simulations of models of CuZr and other binary alloys with effective pairwise interactions that include cohesive energy, atomic symmetry, and atomic size differences to identify the most promising BMG-forming binary alloys.

APPENDIX A: STRUCTURAL CHARACTERIZATION OF ALLOYS FROM CO-SPUTTERING DEPOSITION AND X-RAY DIFFRACTION EXPERIMENTS

We carried out cosputtering and x-ray diffraction experimental studies of crystallization and glass formation in binary, ternary, and multicomponent alloys, containing elements with
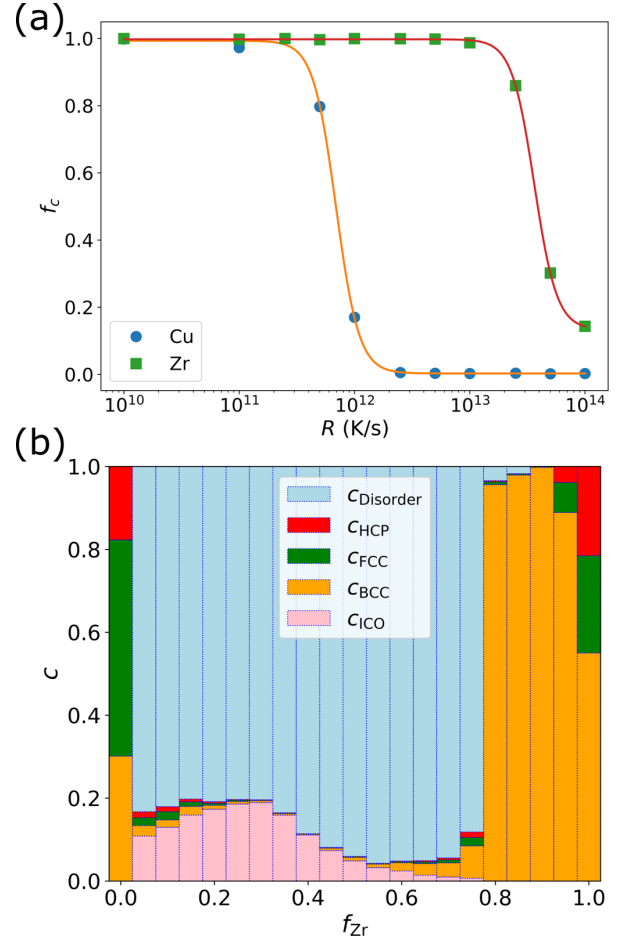

FIG. 14. (a) Fraction of atoms f_c with crystalline order versus cooling rate R from EAM MD simulations of pure Cu and pure Zr. (b) Fraction of atoms c with a given local crystalline order (hcp, fcc, and bcc), icosahedral order (ICO), and other disordered motifs in CuZr alloys versus f_{Zr} from EAM MD simulations obtained from the low-temperature solids at cooling rate $R = 10^{10}$ K/s.

nearly identical sizes. (See Sec. II E for experimental details.) We show the structural characterization results for TiAl alloys in Fig. 12. In Fig. 12(a), we identify the compositions that possess amorphous structures at the characteristic cooling rate 10^9 K/s. In Fig. 12(b), we show the x-ray scattering intensity over a range of f_{Al}. It is clear that even though there is no atomic size difference for TiAl alloys, a wide range of compositions, $0.07 < f_{Al} < 0.82$ form glasses. However, as shown in Fig. 13, all compositions for the Cr-Cu-Ni alloy system (including all NiCu binary alloys) crystallize at the characteristic cooling rate of 10^9 K/s. These results are consistent with our EAM MD simulation studies of NiCu and TiAl binary alloys.

APPENDIX B: EAM MD SIMULATIONS OF CuZr BINARY ALLOYS

We also performed EAM MD simulations of the GFA of CuZr alloys to relate our current studies of binary alloys with

the same-sized atoms, but different cohesive energies and atomic symmetries, to future studies of alloys with different atomic sizes, as well as different cohesive energies and atomic symmetries [54]. Cu has a smaller atomic size and cohesive energy than Zr. Also, Cu forms fcc crystals in equilibrium, and Zr forms hcp crystals. As discussed in the main text, MD simulations of the patchy-particle model predict that pure systems composed of Cu atoms will have better GFAs than pure systems composed of Zr atoms, which is confirmed by the results in Fig. 14(a). In particular, R_c for pure Cu is approximately two orders of magnitude smaller than than that for pure Zr. We also analyzed the local structural order in the low-temperature solid state in CuZr alloys obtained by quenching the high-temperature liquid states at $R = 10^{10}$ K/s over a range of compositions f_{Zr}. As shown in Fig. 14(b), the Zr-rich alloys are more prone to crystallization than the Cu-rich alloys, indicating that the Cu-rich alloys are the better glass formers. In Fig. 14(b), we also show that the fraction of atoms with local ICO order possesses a peak near $f_{Zr} \approx 0.30$, which indicates the composition with the best GFA. Note that the height of the maximum in the fraction of atoms with ICO order depends on the cooling rate $R > R_c$.

[1] G. Kumar, H. X. Tang, and J. Schroers, Nature **457**, 868 (2009).

[2] M. Chen, Annu. Rev. Mater. Res. **38**, 445 (2008).

[3] W. Johnson, Nat. Mater. **14**, 553 (2015).

[4] D. Wang, Y. Li, B. B. Sun, M. L. Sui, K. Lu, and E. Ma, Appl. Phys. Lett. **84**, 4029 (2004).

[5] Y. Sun, A. Concustell, and A. L. Greer, Nat. Rev. Mater. **1**, 16039 (2016).

[6] Y. Li, S. Zhao, Y. Liu, P. Gong, and J. Schroers, ACS Comb. Sci. **19**, 687 (2017).

[7] N. Nishiyama and A. Inoue, Appl. Phys. Lett. **80**, 568 (2002).

[8] A. Inoue, Acta Mater. **48**, 279 (2000).

[9] S. Ding, Y. Liu, Y. Li, Z. Liu, S. Sohn, F. J. Walker, and J. Schroers, Nat. Mater. **13**, 494 (2014).

[10] P. Bordeenithikasem, J. Liu, S. A. Kube, Y. Li, T. Ma, B. E. Scanley, C. C. Broadbridge, J. J. Vlassak, J. P. Singer, and J. Schroers, Sci. Rep. **7**, 7155 (2017).

[11] F. Ren, L. Ward, T. Williams, K. J. Laws, C. Wolverton, J. Hattrick-Simpers, and A. Mehta, Sci. Adv. **4**, eaaq1566 (2018).

[12] M.-X. Li, S.-F. Zhao, Z. Lu, A. Hirata, P. Wen, H.-Y. Bai, M. Chen, J. Schroers, Y. Liu, and W.-H. Wang, Nature **569**, 99 (2019).

[13] Y. Q. Cheng and E. Ma, Prog. Mater. Sci. **56**, 379 (2011).

[14] K. J. Laws, D. B. Miracle, and M. Ferry, Nat. Commun. **6**, 8123 (2015).

[15] Y.-C. Hu, J. Schroers, M. D. Shattuck, and C. S. O'Hern, Phys. Rev. Mater. **3**, 085602 (2019).

[16] E. Perim, D. Lee, Y. Liu, C. Toher, P. Gong, Y. Li, W. N. Simmons, O. Levy, J. J. Vlassak, J. Schroers, and S. Curtarolo, Nat. Commun. **7**, 12315 (2016).

[17] D. Turnbull, Contemp. Phys. **10**, 473 (1969).

[18] K. Zhang, M. Wang, S. Papanikolaou, Y. Liu, J. Schroers, M. D. Shattuck, and C. S. O'Hern, J. Chem. Phys. **139**, 124503 (2013).

[19] L. Zhong, J. Wang, H. Sheng, Z. Zhang, and S. X. Mao, Nature **512**, 177 (2014).

[20] D. Xu, Z. Wang, T.-Y. Chang, and F. Chen, J. Phys. Conden. Matter **32**, 405402 (2020).

[21] R. Ryltsev and N. Chtchelkatchev, Soft Matter **13**, 5076 (2017).

[22] F. Smallenburg and F. Sciortino, Nat. Phys. **9**, 554 (2013).

[23] F. Smallenburg and F. Sciortino, Phys. Rev. Lett. **115**, 015701 (2015).

[24] K. Zhang, Y. Liu, J. Schroers, M. D. Shattuck, and C. S. O'Hern, J. Chem. Phys. **142**, 104504 (2015).

[25] A. M. Halpern, J. Chem. Edu. **89**, 592 (2012).

[26] B. Onat and S. Durukanoğlu, J. Phys. Condens. Matter **26**, 035404 (2013).

[27] R. R. Zope and Y. Mishin, Phys. Rev. B **68**, 024102 (2003).

[28] Z. W. Wu, M. Z. Li, W. H. Wang, and K. X. Liu, Nat. Commun. **6**, 6035 (2015).

[29] M. Tahiri, A. Hasnaoui, and K. Sbiaai, Metall. Mater. Trans. A **49**, 2513 (2018).

[30] P. J. Steinhardt, D. R. Nelson, and M. Ronchetti, Phys. Rev. B **28**, 784 (1983).

[31] A. S. Keys and S. C. Glotzer, Phys. Rev. Lett. **99**, 235503 (2007).

[32] P. Rein ten Wolde, M. J. Ruiz-Montero, and D. Frenkel, J. Chem. Phys. **104**, 9932 (1996).

[33] S. A. Kube, S. Sohn, D. Uhl, A. Datye, A. Mehta, and J. Schroers, Acta Mater. **166**, 677 (2019).

[34] A. Inoue, Prog. Mater. Sci. **43**, 365 (1998).

[35] D. Shechtman, I. Blech, D. Gratias, and J. W. Cahn, Phys. Rev. Lett. **53**, 1951 (1984).

[36] L. C. Chen and F. Spaepen, Nature **336**, 366 (1988).

[37] A. Prokhoda and A. Ovrutsky, arXiv:1403.6668.

[38] H. W. Sheng, Y. Q. Cheng, P. L. Lee, S. D. Shastri, and E. Ma, Acta Mater. **56**, 6264 (2008).

[39] A. Schottelius, F. Mambretti, A. Kalinin, B. Beyersdorff, A. Rothkirch, C. Goy, J. Müller, N. Petridis, M. Ritzer, F. Trinter, J. M. Fernández, T. A. Ezquerra, D. E. Galli, and R. E. Grisenti, Nat. Mater. **19**, 512 (2020).

[40] H. Tanaka, J. Phys. Condens. Matter **15**, L491 (2003).

[41] H. Tanaka, J. Non-Cryst. Solids **351**, 678 (2005).

[42] Y. T. Shen, T. H. Kim, A. K. Gangopadhyay, and K. F. Kelton, Phys. Rev. Lett. **102**, 057801 (2009).

[43] W. L. Johnson, J. H. Na, and M. D. Demetriou, Nat. Commun. **7**, 10313 (2016).

[44] L. Xia, W. H. Li, S. S. Fang, B. C. Wei, and Y. D. Dong, J. Appl. Phys. **99**, 026103 (2006).

[45] H. Tan, Y. Zhang, D. Ma, Y. P. Feng, and Y. Li, Acta Mater. **51**, 4551 (2003).

[46] H.-J. Lee, T. Cagin, W. L. Johnson, and W. A. Goddard, J. Chem. Phys. **119**, 9858 (2003).

[47] F. Guinea, J. H. Rose, J. R. Smith, and J. Ferrante, Appl. Phys. Lett. **44**, 53 (1984).

[48] T. B. Massalski, J. L. Murray, L. H. Bennett, and H. Baker, *Binary Alloy Phase Diagrams* (American Society for Metals, Metals Park, OH, 1986).

[49] Y. Q. Cheng, E. Ma, and H. W. Sheng, Phys. Rev. Lett. **102**, 245501 (2009).

[50] K. Zhang, W. W. Smith, M. Wang, Y. Liu, J. Schroers, M. D. Shattuck, and C. S. O'Hern, Phys. Rev. E **90**, 032311 (2014).

[51] Y. Li, Q. Guo, J. A. Kalb, and C. V. Thompson, Science **322**, 1816 (2008).

[52] Z. Altounian, T. Guo-hua, and J. O. Strom-Olsen, J. Appl. Phys. **53**, 4755 (1982).

[53] J. Ding, Y.-Q. Cheng, and E. Ma, Acta Mater. **69**, 343 (2014).

[54] M. I. Mendelev, M. J. Kramer, R. T. Ott, D. J. Sordelet, D. Yagodin, and P. Popel, Philos. Mag. **89**, 967 (2009).